



Cite this: DOI: 10.1039/d1tc00560j

Nonvolatile organic field-effect transistor memory from pyrene-fused azaindacene regioisomers†

Duan-Wu Liu,^a Yamin Zhang,^{*a} Xiang-Yang Li,^a Qi Xiao,^a Wen-Jing Sun,^a Xiangfeng Shao^{ib}^a and Hao-Li Zhang^{ib}^{*ab}

Nonvolatile memory devices based on organic materials are promising for a new generation of portable or flexible electronics. Herein, two pyrene-fused azaindacene configurational isomers, *syn*-B2IPIO and *anti*-B2IPIO, were designed and synthesized, and they are axially symmetric and centrally symmetric, respectively. These two regioisomers were applied as charge trapping elements (CTEs) for the electret layers in organic field-effect transistor nonvolatile memory (OFET-NVM) devices. Although the two regioisomers have nearly identical molecular structures, absorption spectra, and HOMO/LUMO energy levels, they exhibit distinctly different charge-trapping capabilities. The OFET-NVM devices based on *anti*-B2IPIO exhibit a moderate memory window of about 25 V. In contrast, the devices based on *syn*-B2IPIO show a more than two-fold wider memory window (~59 V). The different charge trapping behaviors of this pair of isomers are attributed to different intermolecular interactions associated with molecular symmetry, resulting in different molecular packing behaviors and film morphologies. The results reveal that controlling the molecular symmetry could be a new and efficient strategy for the design of organic CTEs for high-performance memory devices.

Received 4th February 2021,
Accepted 23rd April 2021

DOI: 10.1039/d1tc00560j

rsc.li/materials-c

Introduction

Memory devices based on organic materials, such as organic memristors,¹ are showing promise for use in a new generation of portable or flexible electronics. Organic field-effect transistor nonvolatile memory (OFET-NVM) devices have attracted great attention recently because of their simple structure, non-destructive readout and high memory performance.^{2,3} Great progress has been made with three main types of OFET-NVMs, namely ferroelectric OFET memories,⁴ floating-gate OFET memories,⁵ and polymer electret OFET memories.⁶ Out of the three types, the OFET-NVMs based on polymer electrets can be manufactured *via* flexible and low-cost processing, and are therefore attractive for practical applications.⁷ Considerable research has been conducted on the fabrication and structure optimization of the electret OFET-NVMs device to achieve a high performance.⁸ However, relatively few comparative studies

have been carried out to gain insight into the structure–property relationship of the organic charge trapping element (CTE) in electret memory devices, so that a good understanding of the material system is still insufficient. Therefore, the design and development of high-performance electret materials are of great importance for the further development of suitable material systems for practical applications.⁹

Research on the dielectric layer of the OFET-NVM is of critical importance for high-performance devices and circuits. For example, Hu and co-workers used 2D mica as a single crystal electret and provided a model system to study the fundamental working mechanism behind the devices.¹⁰ Small aromatic molecules are also ideal CTE materials for the mechanistic study, because of their well-defined structure and tunable electronic properties.¹¹ A variety of solution-processable small molecules have been developed as CTE materials for OFET memory applications, such as fullerene,¹² perylene diimide derivatives,² and so on. Several research groups, including us, have devoted much effort to exploring the structure–property correlation of small aromatic molecule CTE materials. Lee and co-workers reported that a large steric hindrance could produce more charge trapping sites, which can enhance the charge trapping capability of the memory device.¹³ Meanwhile, other research indicated that molecules with small dipole moments are more likely to exhibit high charge trapping behavior in an organic memoristor.¹⁴ Recently, Huang and co-workers suggested that small molecules with non-planar topologies with

^a State Key Laboratory of Applied Organic Chemistry, Key Laboratory of Special Function Materials and Structure Design, College of Chemistry and Chemical Engineering, Lanzhou University, Lanzhou 730000, P. R. China.
E-mail: zym@lzu.edu.cn, haoli.zhang@lzu.edu.cn

^b Tianjin Key Laboratory of Molecular Optoelectronic Sciences, Department of Chemistry, Tianjin University, Collaborative Innovation Center of Chemical Science and Engineering (Tianjin), Tianjin 300072, P. R. China

† Electronic supplementary information (ESI) available. CCDC 2045205. For ESI and crystallographic data in CIF or other electronic format see DOI: 10.1039/d1tc00560j

separated highest occupied molecular orbitals (HOMO) and lowest unoccupied molecular orbitals (LUMO) can provide separate trapping sites for holes and electrons, which may inhibit charge leakage and promote charge trapping.¹⁵

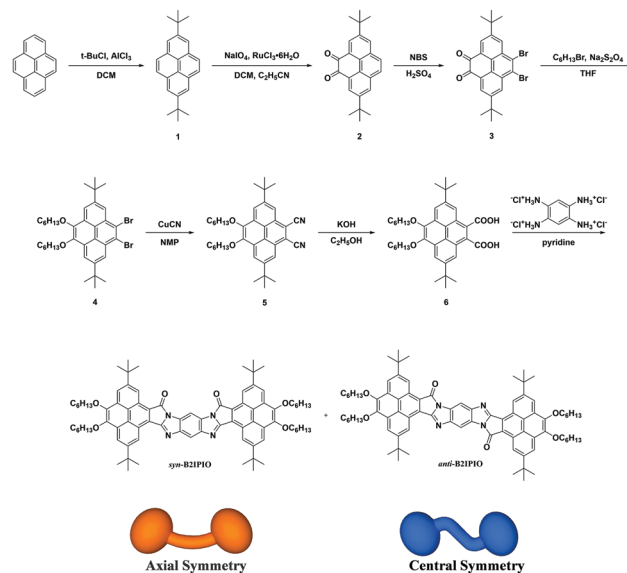
Configurational isomers refer to organic compounds with the same chemical formula but different molecular configurations, which are ideal model systems for the study of structure–property correlation. It is known that many configurational isomers could exhibit significantly different physical properties, including solubility, dipole moment and intermolecular interaction.^{16,17} Importantly, the different molecular symmetries represented by the regioisomers play a key role in solid-state packing. It has been reported that a small variation in molecular symmetry can lead to strong changes in film morphology and charge transfer behavior in OFET devices and OLEDs.^{18,19} However, no systematic effort has been made to evaluate the effects of molecular symmetry in the electret OFET-NVM, so that their roles in organic memory devices remain unclear.

Herein, the design and synthesis of a pair of pyrene-fused azaindacene regioisomers, namely *syn*-B2IPIO and *anti*-B2IPIO, are reported. The two molecules have almost identical molecular structure, except that the *syn*-B2IPIO shows axial symmetry and the *anti*-B2IPIO shows central symmetry. The behavior of these two regioisomers as CTEs for the electret OFET-NVM have been carefully compared. It was found that the molecular symmetry can have a strong impact on charge-trapping ability, resulting in different performance of the memory devices. These results help to further clarify the role of molecular symmetry in organic memory devices, and establish general guidelines for designing high-efficiency CTEs.

Results and discussion

Molecular design and synthesis

Scheme 1 shows the structures and synthetic routes of the two configurational isomers that were designed for this study. Each molecule has two pyrene units fused by an *s*-indacene-like bridge. The pyrene unit was selected because of its high photoluminescence (PL) efficiency and electron-rich planar skeleton.^{20,21} Pyrene-fused pyrazaacene (PPA) and 9,10-imidepyrene-fused pyrazaacene (IPPA) derivatives have been previously reported as n-type doping components for use in high performance memory devices.¹⁴ Here, the rigidization of 2,6-bis(pyren-4-yl)-*s*-indacene fragments ensure the planarity of the π -system. The introduction of electron-withdrawing ketones and multiple N atoms ensures a lower LUMO energy level, and the hexyloxy chain connected to the two pyrene units can improve the processability and crystallinity of the material. The molecular configuration was controlled by the configuration of the azaindacene bridge, and the two configurational isomers were named *syn*-B2IPIO and *anti*-B2IPIO. The *syn*-B2IPIO was axially symmetric and the *anti*-B2IPIO was centrally symmetric. It was hoped that the comparative study of these regioisomers



Scheme 1 The synthetic route to *syn*-B2IPIO and *anti*-B2IPIO.

would help to gain insights into the role of molecular symmetry in the organic memory devices.

The synthesis of the target molecules was based on a regioselective modification of pyrene. Previous work by Zhang and co-workers has revealed that the 4,5,9,10-position (K-region) substituted derivatives of pyrene, such as 9,10-dibromo-2,7-di-*tert*-butylpyrene-4,5-dione (3), can be obtained.²² Using the reduction reaction with sodium hydrosulfite ($\text{Na}_2\text{S}_2\text{O}_4$), two alkyl chains were added to the side of compound 3 to increase the solubility. Then 2,7-di-*tert*-butyl-9,10-bis(hexyloxy)pyrene-4,5-dicarboxylic acid (6) was obtained through cyano substitution and hydrolysis. The target compounds *syn*-B2IPIO and *anti*-B2IPIO were obtained by a dehydration condensation reaction using compound 6 and 1,2,4,5-benzenetetramine tetrahydrochloride. The two isomers were separated by column chromatography. The final yields of the *anti*-B2IPIO and *syn*-B2IPIO were about 10% and 40%, respectively. More detailed synthetic processes are provided in the ESI.† These compounds exhibited good thermal stability with decomposition temperatures over 350 °C under the N_2 atmosphere (see Fig. S4, ESI†), which ensured their stability during the fabrication of the OFET-NVW devices.

The first thing that was noticed was that these two isomers exhibit very different solubilities, which suggests that there were different intermolecular interactions. The *syn*-B2IPIO can be well dissolved in most common organic solvents, which is very advantageous for the preparation of devices by the solution method. In comparison, the *anti*-B2IPIO exhibited a lower solubility than the *syn*-B2IPIO in most solvents, suggesting a stronger intermolecular interaction so that it has a stronger tendency to aggregate in solutions. Fortunately, the single crystal of the *syn*-B2IPIO was obtained by slowly evaporating the mixed solvent of trichloromethane (CHCl_3) and methanol (CH_3OH). The single crystal identification of *syn*-B2IPIO by X-ray crystallographic analysis showed that it adopted a one-dimensional packing mode (shown in Fig. S5, ESI†). Each of

these columns presented a different group of the A–B–A type anti-symmetrical sandwich stacking shape. The crystal structure showed that the *tert*-butyl group in *syn*-B2IPIO hindered the π – π stacking in the solid state, which explained its low tendency to aggregate in solution.

Spectroscopic and electrochemical properties

The optical properties of *syn*-B2IPIO and *anti*-B2IPIO were studied by ultraviolet-visible (UV-vis) spectroscopy and PL spectroscopy in solution and solid film states. In the CHCl_3 solution, *syn*-B2IPIO and *anti*-B2IPIO showed similar absorption peaks (Fig. 1a). The absorption peaks at about 300–350 nm were attributed to the π – π^* transition from the pyrene unit of the compounds, whereas the absorption peaks after 350 nm were attributed to the n – π^* transition of the heteroatom containing an unsaturated part. It is worth noting that the absorption spectrum of the *anti*-B2IPIO showed a red-shift in both the solution and film states when compared with the *syn*-B2IPIO, suggesting that the *anti*-B2IPIO had a stronger intermolecular π – π interaction than *syn*-B2IPIO.²³ Under the excitation wavelength of 430 nm, the *syn*-B2IPIO and *anti*-B2IPIO showed emission peaks at 660 and 665 nm in the CHCl_3 solution, respectively (Fig. 1b). With an increased concentration in solutions, *syn*-B2IPIO showed a smaller peak shift than that of *anti*-B2IPIO (Fig. S1, ESI[†]). In the solid state, the emission spectra *syn*-B2IPIO and *anti*-B2IPIO showed red-shifting by 34 nm and 39 nm, respectively, when comparing with that measured in solutions, as shown in Fig. 1b. More detailed data from the absorption and the emission spectra, as well as the spectra in other polar solvents are provided in Table S1 and Fig. S2 (ESI[†]). In both absorption and emission spectra, the thin films of the two molecules exhibited red shifts when compared with that of the solutions, which indicated that there were stronger intermolecular interactions in the solid state. However, it was noted that the *anti*-B2IPIO exhibited a larger red-shift than *syn*-B2IPIO in both the absorption and the emission spectra, suggesting that the *anti*-B2IPIO had a stronger tendency to aggregate and form a closer packing than *syn*-B2IPIO in the solid-state.²⁴

The HOMO energy levels of the *syn*-B2IPIO and *anti*-B2IPIO were estimated to be -5.66 and -5.62 eV, and their LUMO energy levels were -3.37 and -3.27 eV, respectively. As a result, the corresponding electrochemical band gaps of *syn*-B2IPIO

and *anti*-B2IPIO were estimated to be 2.29 and 2.35 eV, respectively. The cyclic voltammetry (CV) curves of the two compounds are shown in Fig. S3 (ESI[†]) and the detailed electrochemical parameters are listed in Table S1 (ESI[†]). It can be seen that the HOMO energy levels of these two compounds were nearly identical, and the LUMO energy level of the *anti*-B2IPIO was about 0.1 eV lower.

Theoretical calculations

All the calculations were based on the density functional theory (DFT) using the [B3LYP/6-31G(d)] basis set to explore the effect of frontier molecular orbitals and energy levels on charge transport. As shown in Fig. 2a, the LUMO orbitals of the two molecules were concentrated on the imidazole unit of the conjugated skeleton, whereas the HOMO orbitals were delocalized on the entire molecular backbone. As suggested by Huang and co-workers, separation of HOMO and LUMO in the molecules can provide ideal charge capture sites and this can enhance the charge-storing ability of memory devices.¹⁵ In addition, the low-lying LUMO energy level of the two compounds helped to reduce the electron injection barrier from the 6,13-bis(triisopropylsilyl)ethynyl)pentacene (TIPS-pentacene) in the active layer to the electret layer. Conversely, the holes can also overcome the HOMO energy barrier between the TIPS-pentacene and the charge trapping molecule under the negative gate bias and then the electron injection from the TIPS-pentacene into the molecules occurred.

The electrostatic potentials (ESP) were also calculated. As shown in Fig. 2b, the negative charges were mainly located on the nitrogen atoms in the imidazole unit and the carbonyl groups due to their electron-withdrawing property. The central symmetrical structure of *anti*-B2IPIO had a total dipole moment of 0 Debye. The carbonyl groups of *syn*-B2IPIO were located on the same side, which gave it a dipole moment direction mainly along the *Y*-axis, and the total dipole moment was 1.6 Debye. The detailed calculation information for the dipole moments of *syn*-B2IPIO and *anti*-B2IPIO is listed in Table S2 (ESI[†]). It was reported that the dissipation of trapped charges was commonly caused by dipole interactions, and a small dipole moment could help the retention of the charge trapped in the electret

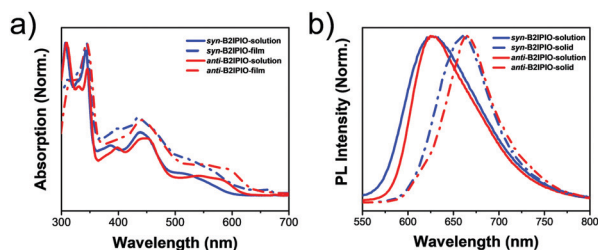


Fig. 1 (a) The UV-vis spectra of *syn*-B2IPIO and *anti*-B2IPIO in CHCl_3 solutions and in thin films. (b) The PL spectra of *syn*-B2IPIO and *anti*-B2IPIO in CHCl_3 solutions and in solid phases (excitation wavelength: 430 nm).

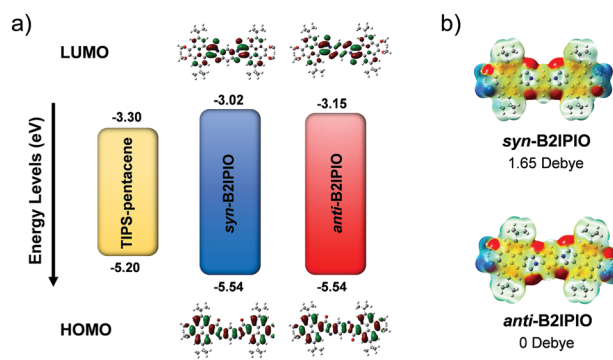


Fig. 2 (a) The HOMO and LUMO energies calculated with DFT at the B3LYP/6-31G(d) level, and (b) the ESP and dipole moments of *syn*-B2IPIO and *anti*-B2IPIO.

layer which improved the memory performance of the device.^{14,25} The total dipole moments of *syn*-B2IPIO and *anti*-B2IPIO were both small, and therefore can avoid the occurrence of dissipation of trapped charges, which enabled them to become effective doping materials for OFET memories.

Thin film morphologies

The film morphology of the organic layer had a significant impact on the performance of organic electronic devices.²⁶ A smooth interface was an important factor for the further growth and crystallization of the atop semiconductor layer, which facilitated charge injection.²⁷ Herein, transmission electron microscopy (TEM) images were used to study the films of *syn*-B2IPIO and *anti*-B2IPIO doped polystyrene (PS) with different ratios, where the dark spots, shown in Fig. 3b, represented the aggregation of *anti*-B2IPIO. Compared with the TEM image of pure PS shown in Fig. S7a (ESI[†]), *syn*-B2IPIO showed almost no aggregation behavior at 0.5% and 1% blending ratios. When the blending ratio increased to 3%, a small number of dark

spots were found (Fig. S8b, ESI[†]). However, obvious small black spots can be observed in the TEM image of the PS film doped with 0.5% *anti*-B2IPIO (Fig. S8c, ESI[†]). The blend films doped with 1% or 3% *anti*-B2IPIO showed very dense aggregation spots, which indicated that *anti*-B2IPIO did not have good dispersibility in PS. Atomic force microscopy (AFM) was also used to study the film morphology of the electret layer. Fig. 3c shows that the thin film of PS blended with the *syn*-B2IPIO (*syn*-B2IPIO@PS) presented a smooth, uniform, and hydrophobic surface. No phase segregation of the mixed film occurred during the spin coating process, which was mainly due to the high solubility and weak aggregation behaviors of *syn*-B2IPIO. The root-mean-square (RMS) roughness of the electret blend film was 0.36 nm on 5 $\mu\text{m} \times 5 \mu\text{m}$ areas, which was close to that of pure PS film (Fig. S7b, ESI[†]), and this indicated that low concentration doping has little effect on the electret layer surface morphology. The PS *anti*-B2IPIO blend (*anti*-B2IPIO@PS) film showed the highest roughness of 0.60 nm (Fig. 3d), which was slightly higher than that of *syn*-B2IPIO@PS, which indicated that the *anti*-B2IPIO may have a certain degree of aggregation in the film. Water contact angles of the *syn*-B2IPIO@PS and *anti*-B2IPIO@PS films were 96.86° and 95.99°, respectively, as shown in the insets of Fig. 3c and d. The hydrophobic surfaces ensure face-on growth of TIPS-pentacene on the electret surface.

Optical microscopy and fluorescence microscopy studies showed that the blend film of *syn*-B2IPIO@PS presented a smooth and uniform surface (Fig. S6a and c, ESI[†]). However, there were microscopic particles distributed in the *anti*-B2IPIO@PS blend film, which emitted red light when excited (Fig. S6b and d, ESI[†]), indicating that significant aggregation had taken place. It has been reported that the phase segregation in the blend film affects the charge trapping ability of the doped electret layers.²⁸ The lower solubility and higher crystallinity property of the *anti*-B2IPIO made it aggregate more easily during the spin coating process, which resulted in phase segregation. In contrast, the *syn*-B2IPIO@PS blend films show a weak phase segregation tendency, which is favorable for charge storage.

Film morphologies of the TIPS-pentacene deposited on the blend films by vacuum thermal evaporation were also studied by AFM. The TIPS-pentacene crystal domain grown on the blend film was about 0.2–0.3 μm (Fig. 3e and f). The small domain size may be ascribed to the fact that the dielectric surface hindered the lateral diffusion of TIPS-pentacene and inhibited the continuity of the TIPS-pentacene arrangement. In addition, X-ray diffraction (XRD) was also used to study the crystal morphology of the TIPS-pentacene layer. The XRD pattern of the TIPS-pentacene film showed a series of peaks, corresponding to the reflections of (001) and (11–5) (see Fig. S11, ESI[†]), which indicated that the TIPS-pentacene on different electret layers had a high crystallinity in the same crystal phase.

Memory device characteristics

As TIPS-pentacene was used as the active layer of the device, all the devices showed the characteristic curve of p-type

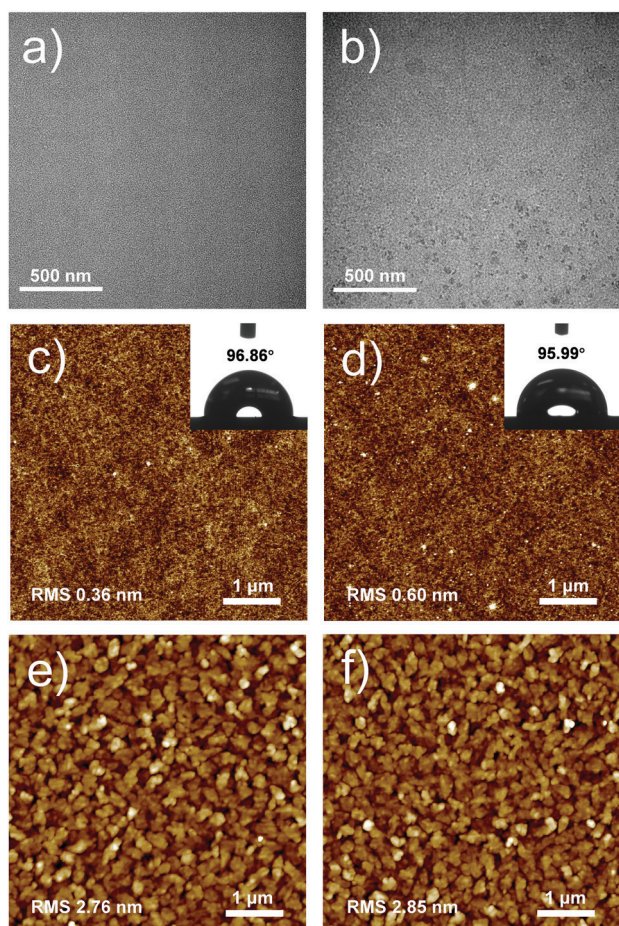


Fig. 3 TEM images of (a) 1% *syn*-B2IPIO@PS and (b) 1% *anti*-B2IPIO@PS blend films. AFM topographic images of (c) 1% *syn*-B2IPIO@PS and (d) 1% *anti*-B2IPIO@PS blend films on SiO₂/Si substrates, in 5 $\mu\text{m} \times 5 \mu\text{m}$ areas. The insets of (c) and (d) are the contact angles of the B2IPIO@PS film surfaces (side view of a drop of water). AFM topographic images of TIPS-pentacene crystallized on the surface of (e) *syn*-B2IPIO@PS and (f) *anti*-B2IPIO@PS, in 5 $\mu\text{m} \times 5 \mu\text{m}$ areas.

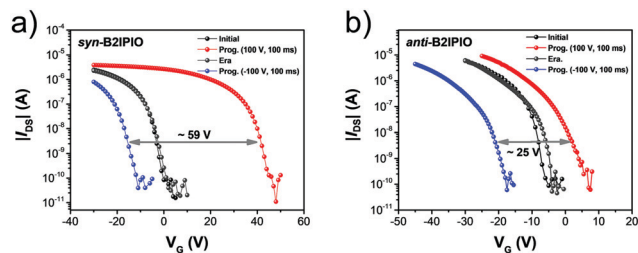


Fig. 4 Characteristic transfer curves of memory devices with (a) 1% *syn*-B2IPIO@PS blend film and (b) 1% *anti*-B2IPIO@PS blend film as electret layers. V_{DS} is -30 V.

transistors, as shown in Fig. S14 (ESI[†]). The OFET mobility of the devices was maintained at about $0.05 \text{ cm}^2 \text{ V}^{-1} \text{ s}^{-1}$, which was comparable to the TIPS-pentacene mobility, obtained using the same evaporation method, reported in the literature.²⁹

Fig. 4 shows the positive and negative shifts of the transfer curves doped with the *syn*-B2IPIO and *anti*-B2IPIO when the drain-source voltage was -30 V. After applying a positive gate bias ($V_G = 100$ V, 100 ms), the transfer curves shifted in a positive direction, which was the positive “programming” process. In order to further verify whether memory devices based on the *syn*-B2IPIO and *anti*-B2IPIO could be effectively erased, the corresponding reverse gate bias was applied after the trial programming. It was worth noting that when the negative gate bias voltage was greater than -80 V, all the devices were completely erased, which showed that the device exhibited hole trapping capabilities. Subsequently, a negative gate bias ($V_G = -100$ V, 100 ms) was applied to the devices, and it was set to the negative “programming” process. The memory window (ΔV_{th}) is defined as the difference between the V_{th} of the programming and erasing states. Both *syn*-B2IPIO and *anti*-B2IPIO exhibited charge storage capacity, and the total memory windows obtained were higher than that of pure PS memory devices (Fig. S15, ESI[†]), which are approximately 59 and 25 V, respectively, in electron (100 V) and hole (-100 V) capture modes. In the programming process, the programming time of the *syn*-B2IPIO-doped device was gradually changed, and the ΔV_{th} did not change significantly (Fig. S18a, ESI[†]). This phenomenon showed that *syn*-B2IPIO provided a strong capture site, thus exhibiting a fast capture speed. In addition, OFET memory devices based on PS films blended with 0.5% and 3% of *syn*-B2IPIO and *anti*-B2IPIO as charge trapping layers were also fabricated to investigate the change of the memory windows (see Fig. S16, ESI[†]). The transistor and memory characteristics of various wt% B2IPIO are shown in Table S5 (ESI[†]). Although the memory windows changed under different doping concentrations, devices based on *syn*-B2IPIO always showed better charge trapping capabilities than those of *anti*-B2IPIO.

This result showed that the memory parameter values were mainly determined by the intrinsic properties of the dopant. Table S6 (ESI[†]) compares the memory windows of the OFET-memory devices prepared in this work with those reported in the literature,^{33–39} which indicated that *syn*-B2IPIO was one of the best materials reported to date.

The shift of ΔV_{th} under different programming voltages (V_{Prog}) was compared to further determine the trapping behavior. When the positive gate bias voltages of 60, 80, 100, and 120 V were applied, the transfer curve of the *syn*-B2IPIO based device shifted with the increase of the gate bias, showing multibit memory windows of 15.8, 31.6, 45.1 and 55.2 V (Fig. S17a, ESI[†]). When the negative gate voltage is greater than -60 V, the *syn*-B2IPIO based memory device also undergoes a similar negative movement (Fig. S17b, ESI[†]), which indicates the devices based on *syn*-B2IPIO can perform multibit memory functions in one unit to achieve high memory density. The shifts of ΔV_{th} with different V_{Prog} are plot in Fig. S17e (ESI[†]). All the devices based on the *syn*-B2IPIO show an approximate linear fit with ΔV_{th} as a function of V_{Prog} , which was consistent with the Fowler–Nordheim tunneling model.³⁰ Moreover, the slope of the *syn*-B2IPIO was larger at a low voltage, indicating that the electronic storage capacity was stronger than that of the *anti*-B2IPIO.

The following equation:

$$\Delta n = \Delta V_{th} \times \frac{C_i}{e} \quad (1)$$

is used to calculate charge trapping density (Δn), where e is the element charge (1.602×10^{-19} C), C_i is the total capacitance per unit area (calculated from the equation: $C_i = 1/C_M + 1/C_{SiO_2}$). The Δn of the memory devices indicated that when the positive gate bias (100 V) and negative gate bias (-100 V) were applied, the devices showed electron and hole trapping capabilities, respectively. More importantly, the *syn*-B2IPIO had a high electron capture density, and thus exhibits better charge memory performance. Table 1 summarizes the characteristics of memory devices based on the 1% doped *syn*-B2IPIO and

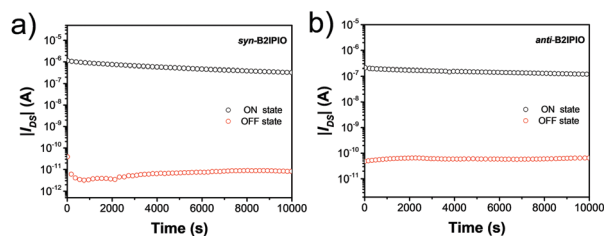


Fig. 5 Data retention of the memory devices with (a) 1% *syn*-B2IPIO@PS blend film and (b) 1% *anti*-B2IPIO@PS blend film as the electret layer.

Table 1 Parameters of OFET memory devices

Compound	μ [$\text{cm}^2 \text{ V}^{-1} \text{ s}^{-1}$]	V_{th} [V]	Capacitance [nF cm^{-2}]	I_{ON}/I_{OFF}	Memory window [V]	Δn [10^{12} cm^{-2}]
1% <i>syn</i> -B2IPIO	0.058 (0.043)	-1.3 (-3.6)	9.58	$> 10^5$	59.2 (53.4)	3.54 (3.19)
1% <i>anti</i> -B2IPIO	0.061 (0.036)	-3.9 (-6.8)	8.87	$> 10^4$	25.5 (22.3)	1.41 (1.23)

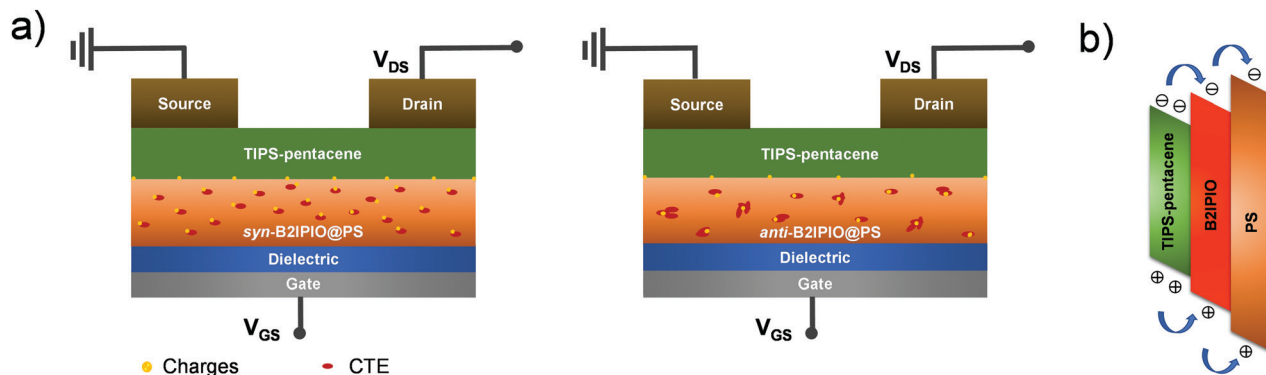


Fig. 6 (a) Schematic diagrams of the configurations of OFET-NVM devices based on *syn*-B2IPIO (left) and *anti*-B2IPIO (right), and (b) an illustration of charge transfer in the OFET-NVM device.

anti-B2IPIO, where each average value was obtained from more than 20 working devices.

Reversibility and retention behaviors

The memory characteristics of the devices were evaluated by the retention time tests. Retention time is a key indicator of the stability of charge storage, and it reflects the time that the charge remains in the charge trap layer. Fig. 5 shows that all the devices exhibited good retention characteristics. The I_{DS} could be maintained for at least 10^4 s with a V_{DS} of -30 V. The on/off ratio gradually decreased with time, which was mainly due to the increase in the cut-off current. Due to the high mobility of the memory devices, the on/off ratio of the *syn*-B2IPIO based memory devices was maintained at 10^5 during the test time range. Write-read-erase-read (WRER) cycles of the memory devices showed stable switching behaviors of more than 100 times, indicating that these devices can maintain good reversibility, as shown in Fig. S19 (ESI[†]). These results illustrate the excellent data retention performance of memory devices doped with *syn*-B2IPIO and *anti*-B2IPIO.

It is worth noting that the rational design of small molecule CTEs for improved the charge storage density and endurance is still a challenge. Several factors have been discussed in previous reports in the literature that may affect the performance of memory devices, such as molecular energy level, dipole moments, intermolecular interactions, and molecular packing.^{31,32} Herein, particular attention was paid to the effects of molecular symmetry. In this research it was demonstrated that the *syn*-B2IPIO and *anti*-B2IPIO, which have nearly identical structure but different molecular symmetry, exhibited distinctly different charge storage performances. This was attributed to the observed molecular symmetry effects of the symmetry-induced differences in the intermolecular π - π interaction, which was reflected in their different solubility and aggregation behaviors. During the solution-based device fabrication, a higher solubility helped to produce ideal film morphology that facilitated the charge injection from the organic semiconductor layer into the electret layer (Fig. 6a and b). Although efforts were made to improve the solubility of *anti*-B2IPIO in solution and optimize the film casting conditions, it

was still difficult to totally avoid aggregation in the blend film. The relatively weaker intermolecular π - π interaction of *syn*-B2IPIO avoided molecular aggregation in the blend films and that provided more charge trapping sites and improved the charge trapping density. As a result, the OFET-NVM based on the *syn*-B2IPIO showed a much higher memory performance than the devices based on *anti*-B2IPIO.

Conclusions

In summary, two pyrene-fused azaindacene configurational isomers, *syn*-B2IPIO and *anti*-B2IPIO, were designed and synthesized *via* an effective synthetic method. These two isomers have same molecular formulae and similar absorption spectra and HOMO/LUMO energy levels. However, when used as CTEs in OFET-NVM devices, they exhibit very different charge-trapping capabilities. OFET-NVM devices based on *syn*-B2IPIO show a much wider memory window (~ 59 V) and higher charge trapping density than those based on *anti*-B2IPIO. In this system, axisymmetric *syn*-B2IPIO exhibits high solubility and moderate intermolecular interactions and, consequently, much superior performance as a CTE material when compared with centrosymmetric *anti*-B2IPIO. This investigation reveals that molecular symmetry can play a crucial role in the charge capture behaviors of CTEs in OFET-NVMs. Therefore, careful structural design and the optimization of molecular symmetry are essential for future molecular design for high-performance organic memory devices.

Experimental

Chemicals and materials

Unless otherwise stated, all solvents and chemicals were obtained from commercial sources (TCI America or J&K Chemicals) without further purification. The $^1\text{H-NMR}$ and $^{13}\text{C-NMR}$ spectra were recorded on a Bruker AVANCE III 400 MHz/600 MHz instrument using CDCl_3 as the solvent and the measurements were carried out at room temperature. Mass spectrometry (MS) data were obtained with a Bruker Esquire 6000 mass spectrometer with an ESQ6K operator. The thermal

properties of the compounds were examined by thermogravimetric analysis (TGA) on a Linseis STA PT 1600. The heating rate was $10\text{ }^{\circ}\text{C min}^{-1}$ under a flowing N_2 atmosphere. Single crystal X-ray diffraction measurements were conducted on a Bruker D8 VENTURE Kappa Duo PHOTON II CPAD diffractometer with graphite-monochromatized $\text{Cu K}\alpha$ radiation ($\lambda = 1.54184\text{ \AA}$) under a flowing N_2 atmosphere.

Spectroscopic and electrochemical measurements

The UV-vis and PL spectroscopy of *syn*-B2IPIO and *anti*-B2IPIO in CHCl_3 solutions and films were measured using a Persee T6 UV-vis spectrometer (Purkinje General, China) and a FLS920 fluorescence spectrometer (Edinburgh Instruments, UK). The frontier molecular orbital energy levels of the compounds were estimated using CV. The oxidation potentials and reduction potentials were measured in anhydrous CH_2Cl_2 solution (1.0 mM), in which 0.1 M tetrabutylammonium hexafluorophosphate (TBAPF_6) was the supporting electrolyte, a glassy carbon electrode was the working electrode, a platinum wire was the counter electrode, and an Ag/AgCl electrode was the reference electrode. The extent of aggregation of B2IPIO was visualized using a ThermoScientific Talos F200S transmission electron microscope (TEM) operated at an acceleration voltage of 200 kV.

Fabrication of OFET-NVM devices

The OFET-NVM devices were constructed using the bottom-gate and top-contact structure. Highly doped n-type Si (100) wafers with 300 nm thick SiO_2 were used as the substrate. PS was dissolved in toluene at a concentration of 4 mg/mL and stirred overnight. The *syn*-B2IPIO and *anti*-B2IPIO compounds were dissolved in the solution at a concentration of 1 wt%. Subsequently, the filtered, mixed solution was spin-coated on the SiO_2 wafer at 3000 rpm for 30 s, and then annealed at $80\text{ }^{\circ}\text{C}$ for 30 min. Tips-pentacene was thermally deposited to the thickness of 25 nm with a deposition rate of 0.1 nm s^{-1} under vacuum ($3.0 \times 10^{-4}\text{ Pa}$). A layer of 50 nm Ag was then deposited onto the substrate by thermal evaporation ($3.0 \times 10^{-4}\text{ Pa}$) through a shadow mask. The channel width (W) and the channel length (L) were 800 μm and 60 μm , respectively. The cross-sectional scanning electron microscope (SEM) images indicated the clearly layered structure of the memory devices, as shown in Fig. S12 (ESI[†]). The transfer and output characteristics of the device were tested in a glove box using a Keithley Instruments, 4200-SCS parameter analyser.

Conflicts of interest

There are no conflicts to declare.

Acknowledgements

This work was supported by the National Key R&D Program of China (2017YFA0204903), the National Natural Science Foundation of China (NSFC, 51733004, 22075117, 22073038, 21602093,

22005128), the 111 Project, and the Fundamental Research Funds for the Central Universities (lzujbky-2020-44).

Notes and references

- 1 Y. Liu, Y. Yang, D. Shi, M. Xiao, L. Jiang, J. Tian, G. Zhang, Z. Liu, X. Zhang and D. Zhang, *Adv. Mater.*, 2019, **31**, 1902576.
- 2 W. Li, F. Guo, H. Ling, P. Zhang, M. Yi, L. Wang, D. Wu, L. Xie and W. Huang, *Adv. Sci.*, 2017, **4**, 1700007.
- 3 Y. J. Jeong, D.-J. Yun, S. H. Noh, C. E. Park and J. Jang, *ACS Nano*, 2018, **12**, 7701–7709.
- 4 Q. Zhao, H. Wang, Z. Ni, J. Liu, Y. Zhen, X. Zhang, L. Jiang, R. Li, H. Dong and W. Hu, *Adv. Mater.*, 2017, **29**, 1701907.
- 5 C. Yan, J. Wen, P. Lin and Z. Sun, *Small*, 2019, **15**, 1804156.
- 6 Y.-C. Chiu, T.-Y. Chen, C.-C. Chueh, H.-Y. Chang, K. Sugiyama, Y.-J. Sheng, A. Hirao and W.-C. Chen, *J. Mater. Chem. C*, 2014, **2**, 1436–1446.
- 7 J. Aimi, P.-H. Wang, C.-C. Shih, C.-F. Huang, T. Nakanishi, M. Takeuchi, H.-Y. Hsueh and W.-C. Chen, *J. Mater. Chem. C*, 2018, **6**, 2724–2732.
- 8 A. Cui, Z. Liu, H. Dong, F. Yang, Y. Zhen, W. Li, J. Li, C. Gu, X. Zhang, R. Li and W. Hu, *Adv. Mater.*, 2016, **28**, 8227–8233.
- 9 W. Hu, H. Zhang, K. Salaita and H. Sirringhaus, *SmartMat*, 2020, **1**, e1014.
- 10 X. Zhang, Y. He, R. Li, H. Dong and W. Hu, *Adv. Mater.*, 2016, **28**, 3755–3760.
- 11 S. Miao, H. Li, Q. Xu, N. Li, J. Zheng, R. Sun, J. Lu and C. M. Li, *J. Mater. Chem.*, 2012, **22**, 16582–16589.
- 12 Y. Zhou, S.-T. Han, Y. Yan, L.-B. Huang, L. Zhou, J. Huang and V. A. L. Roy, *Sci. Rep.*, 2013, **3**, 3093.
- 13 M.-H. Jung, K. H. Song, K. C. Ko, J. Y. Lee and H. Lee, *J. Mater. Chem.*, 2010, **20**, 8016–8020.
- 14 Z.-H. Wu, W.-J. Sun, H.-H. Tian, Z.-F. Yu, R.-X. Guo, X. Shao and H.-L. Zhang, *Adv. Electron. Mater.*, 2019, **5**, 1800598.
- 15 Y. Yu, L.-Y. Bian, J.-G. Chen, Q.-H. Ma, Y.-X. Li, H.-F. Ling, Q.-Y. Feng, L.-H. Xie, M.-D. Yi and W. Huang, *Adv. Sci.*, 2018, **5**, 1800747.
- 16 M. Romain, D. Tondelier, J. C. Vanel, B. Geffroy, O. Jeannin, J. Rault-Berthelot, R. Métévier and C. Poriol, *Angew. Chem., Int. Ed.*, 2013, **52**, 14147–14151.
- 17 J. L. Marshall, N. J. O'Neal, L. N. Zakharov and M. M. Haley, *J. Org. Chem.*, 2016, **81**, 3674–3680.
- 18 C. Zhang, Y. Zang, E. Gann, C. R. McNeill, X. Zhu, C.-A. Di and D. Zhu, *J. Am. Chem. Soc.*, 2014, **136**, 16176–16184.
- 19 D. Zhang, X. Song, M. Cai, H. Kaji and L. Duan, *Adv. Mater.*, 2018, **30**, 1705406.
- 20 F. Moggia, C. Videlot-Ackermann, J. Ackermann, P. Raynal, H. Brisset and F. Fages, *J. Mater. Chem.*, 2006, **16**, 2380.
- 21 H. Wang, D. Zhang, X. Guo, L. Zhu, Z. Shuai and D. Zhu, *Chem. Commun.*, 2004, 670–671.
- 22 Z. H. Wu, Z. T. Huang, R. X. Guo, C. L. Sun, L. C. Chen, B. Sun, Z. F. Shi, X. Shao, H. Li and H. L. Zhang, *Angew. Chem., Int. Ed.*, 2017, **56**, 13031–13035.

- 23 D. Shi, Z. Liu, J. Ma, Z. Zhao, L. Tan, G. Lin, J. Tian, X. Zhang, G. Zhang and D. Zhang, *Adv. Funct. Mater.*, 2020, **30**, 1910235.
- 24 J. Lin, W. Li, Z. Yu, M. Yi, H. Ling, L. Xie, S. Li and W. Huang, *J. Mater. Chem. C*, 2014, **2**, 3738–3743.
- 25 C. Sun, Z. Lin, W. Xu, L. Xie, H. Ling, M. Chen, J. Wang, Y. Wei, M. Yi and W. Huang, *J. Phys. Chem. C*, 2015, **119**, 18014–18021.
- 26 Y.-C. Chiu, T.-Y. Chen, Y. Chen, T. Satoh, T. Kakuchi and W.-C. Chen, *ACS Appl. Mater. Interfaces*, 2014, **6**, 12780–12788.
- 27 C. Zheng, T. Tong, Y. Hu, Y. Gu, H. Wu, D. Wu, H. Meng, M. Yi, J. Ma, D. Gao and W. Huang, *Small*, 2018, **14**, 1800756.
- 28 W. Li, F. Guo, H. Ling, H. Liu, M. Yi, P. Zhang, W. Wang, L. Xie and W. Huang, *Small*, 2018, **14**, 1701437.
- 29 S. K. Park, T. N. Jackson, J. E. Anthony and D. A. Mourey, *Appl. Phys. Lett.*, 2007, **91**, 063514.
- 30 Y. Guo, C.-a. Di, S. Ye, X. Sun, J. Zheng, Y. Wen, W. Wu, G. Yu and Y. Liu, *Adv. Mater.*, 2009, **21**, 1954–1959.
- 31 R. Noriega, J. Rivnay, K. Vandewal, F. P. V. Koch, N. Stingelin, P. Smith, M. F. Toney and A. Salleo, *Nat. Mater.*, 2013, **12**, 1038–1044.
- 32 K. Schmidt, C. J. Tassone, J. R. Niskala, A. T. Yiu, O. P. Lee, T. M. Weiss, C. Wang, J. M. J. Fréchet, P. M. Beaujuge and M. F. Toney, *Adv. Mater.*, 2014, **26**, 300–305.
- 33 L. Song, Y. Wang, Q. Gao, Y. Guo, Q. Wang, J. Qian, S. Jiang, B. Wu, X. Wang, Y. Shi, Y. Zheng and Y. Li, *ACS Appl. Mater. Interfaces*, 2017, **9**, 18127–18133.
- 34 L. A. Frolova, A. A. Rezvanova, V. Z. Shirinian, A. G. Lvov, A. V. Kulikov, M. M. Krayushkin and P. A. Troshin, *Adv. Electron. Mater.*, 2016, **2**, 1500219.
- 35 K.-J. Baeg, Y.-Y. Noh, H. Sirringhaus and D.-Y. Kim, *Adv. Funct. Mater.*, 2010, **20**, 224–230.
- 36 Y. Wang, Y. Yang, P. Ding, Q. Wei, X. Gao, S. Wang, C. Liu, A. Li, J. Yin, Y. Xia and Z. Liu, *Adv. Electron. Mater.*, 2019, **5**, 1800865.
- 37 S.-J. Kim and J.-S. Lee, *Nano Lett.*, 2010, **10**, 2884–2890.
- 38 Y. Park, K.-J. Baeg and C. Kim, *ACS Appl. Mater. Interfaces*, 2019, **11**, 8327–8336.
- 39 M. Martínez-Abadía, G. Antoncilli, E. Zuccatti, A. Atxabal, M. Melle-Franco, L. E. Hueso and A. Mateo-Alonso, *Org. Lett.*, 2017, **19**, 1718–1721.